Supporting Information for: Measured ice nucleating particle concentrations improve the simulation of mid-level mixed-phase clouds over the high-latitude Southern Ocean

É. Vignon[1], S. P. Alexander[2,3], P. J. DeMott[4],

G. Sotiropoulou[5,6], F. Gerber[7,8], T. C. J. Hill[4], R. Marchand[9],

A. Nenes[5,10]and A. Berne[1]

[1]Environmental Remote Sensing Laboratory (LTE), École Polytechnique Fédérale de Lausanne (EPFL), Lausanne, Switzerland

[2]Australian Antarctic Division, Kingston, Tasmania, Australia

[3]Australian Antarctic Program Partnership, Institute for Marine and Antarctic Science, University of Tasmania, Hobart, Australia

[4]Department of Atmospheric Science, Colorado State University, Fort Collins

[5]Laboratory of Atmospheric Processes and their Impacts (LAPI), Ecole Polytechnique Fédérale de Lausanne (EPFL), Lausanne, Switzerland

[6]Department of Meteorology and Bolin Center for Climate Research, Stockholm University, Stockholm, Sweden

[7]Laboratory of Cryospheric Sciences, School of Architecture, Civil and Environmental Engineering, École Polytechnique Fédérale de Lausanne (EPFL), Lausanne, Switzerland

[8]WSL Institute for Snow and Avalanche Research SLF, Davos, Switzerland

[9]Department of Atmospheric Sciences, University of Washington, Seattle, WA, USA

[10]ICE-HT, Foundation for Research and Technology Hellas (FORTH), Patras, Greece

Contents of this file

1. Estimating the turbulent kinetic energy dissipation from Doppler radar data

From measurements with a cloud Doppler radar like the MWACR, it is possible to derive the rate of TKE dissipation within clouds. We applied a similar methodology as in M. D. Shupe, Kollias, Persson, and McFarquhar (2008) and M. Shupe, Brooks, and Canut (2012) for Arctic stratocumulus. The principle is described in Bouniol, Illingworth, and Hogan (2004) and Lothon, Lenschow, Leon, and Vali (2005) and summarized in M. Shupe et al. (2012). We briefly recap it herebelow. The variance of the mean Doppler velocity σ_m^2 estimated over a given integration time length Δt reads as the sum of three terms:

$$\sigma_m^2 = \sigma_w^2 + \sigma_{v_f}^2 + 2\mathrm{cov}(w, v_f) \quad (1)$$

where σ_w^2 is the variance of turbulent vertical motions and $\sigma_{v_f}^2$ is the variance of the particle fall velocity within the radar volume. For turbulent but weakly precipitating clouds such as drizzling stratocumulus or mixed-phase stratocumulus, $\sigma_{v_f}^2$ is usually negligible compared to σ_w^2 (Lothon et al., 2005; M. Shupe et al., 2012). First-order estimations using typical ice particle size distributions and diameter-fallspeed relationships as well as TKE values found in WRF simulations show that $\sigma_m^2 >> \sigma_{v_f}^2$ also holds at the top part of altocumulus analysed in the present study (not shown). The exact procedure for the $\sigma_{v_f}^2$ calculation can be found in Doviak and Zrnic (1993). The covariance term in eq. 1 is much more difficult to estimate. However, M. Shupe et al. (2012) show that for stratiform arctic clouds, the covariance acts mostly on scales larger than the scales important for dissipation of turbulence (inertial subrange). If the integration period over which σ_m is

estimated is short enough not to fully sample non-turbulent meso-scale motions, we can fairly neglect this term in eq. 1.

One can therefore write:

$$\sigma_m^2 = \sigma_w^2 \tag{2}$$

Further assuming that turbulence in clouds occurs in near-neutral conditions, the application of the Kolmogorov's theory in the inertial subrange gives:

$$\sigma_w^2 = \int_{k1}^{k2} S(k)dk \tag{3}$$

where $S(k) = \kappa\epsilon k$ is the turbulence spectrum in the inertial subrange with k the wave number of turbulent motions, α the Kolomogorov constant and ϵ the TKE dissipation rate. $k_1 = 2\pi/L_1$ and $k_2 = 2\pi/L_2$ with L_1 and L_2 two length scales of interest in the inertial subrange. L_1 characterizes the size of the largest eddies sampled by the radar during the time integration over $\Delta t = 60$ s. L_2 is related to the scattering volume dimension sampled during the radar dwell time of the MWACR $\delta t = 2$ s (Kollias et al., 2016). Using eq. 2 and developing eq. 3, one ends up with:

$$\sigma_m^2 = \frac{3\alpha}{2}\frac{\epsilon}{2\pi}^{2/3}(L_1^{2/3} - L_2^{2/3}) \tag{4}$$

equation with which we can retrieve ϵ by replacing σ_m with the measured value. Assuming Taylor's frozen turbulence hypothesis, L_1 and L_2 can be expressed as functions of the sampling volume geometry and wind speed: $Ut + 2R\sin(\theta_R)$. R is the range to the radar volume, θ_R is the radar beamwidth, t is either Δt or δt (for L_1 and L_2 respectively) and U is the wind speed estimated from radiosonde measurements. Note that the wind speed at each altitude is linearly interpolated in time between 6-hourly radiosoundings. In any case, our analysis of ϵ has been restricted to periods close to sounding launch times.

2. CCN measurements and estimation of the cloud droplet number concentration

The concentration of cloud condensation nuclei (CCN) for different supersaturation values were also measured on the ship at a frequency of 1 Hz using a continuous-flow streamwise thermal-gradient chamber (Roberts & Nenes, 2005). The dataset is available at `https://www.arm.gov/capabilities/instruments/ccn`. CCN concentration is measured for different supersaturation values (0, 0.1, 0.2, 0.5, 0.8 and 1 %). Measurement affected by exhausts of the ship have been removed using the exhaust detection dataset from Humphries (2019).

In the Morrison microphysical scheme of WRF, one has to set the number concentration of cloud droplet to a fixed value. From airborne measurements of clouds above the Weddell Sea - consisting mostly in boundary-layer clouds but frontal clouds were also sampled - (O'Shea et al., 2017) obtain a median droplet concentration of $N_c = 113$ cm^{-3} and an interquartile range of 86 cm^{-3}. Over the Antarctic Peninsula, Lachlan-Cope, Listowski, and O'Shea (2016) show cloud droplet concentrations between 60 and 200 cm^{-3}. In view of those studies, a N_c value of approximately 100 cm^{-3} seems reasonable for our study. We can try to verify whether this value is consistent with the above CCN measurements even though this verification step will be limited to boundary-layer atmospheric conditions.

Figure S1a shows the distribution of the CCN concentration at 0.1, 0.2 and 0.5 % supersaturation during the study case period. To estimate the droplet number concentration from CCN measurements, one has to estimate the supersaturation occurring within the air parcels in which supercooled liquid droplets activate and grow. Supersaturation mostly depends on the vertical velocity of updrafts and on the concentration of ice crystals thereof (A. V. Korolev & Mazin, 2003; A. Korolev et al., 2017). Figure S1b shows the distribution of the Doppler velocity measured by MWACR conditioned to regions where

the MPL detects SLW. The Doppler velocity reflects the net vertical velocity of the particles i.e. the sum of their respective terminal fallspeed and the vertical wind. Assuming that ice crystals in the mixed-phase air parcels have a fallspeed close to -0.5 ms^{-1} (which roughly corresponds to the mean value of the Doppler velocity distribution, -0.45 ms^{-1}), Figure S1b shows that updrafts containing droplets have a velocity comprised between 0 and 1.5 ms^{-1}. SLW can be created and maintained only in sufficiently strong updrafts i.e. whose vertical velocity exceeds a threshold value (A. V. Korolev, 2008). Considering realistic values of ice crystal size and concentration for Antarctic conditions, the supersaturation in sufficiently strong updrafts generally ranges between 0.05 et 0.35 % (formulae for supersaturation and threshold vertical velocity calculations are taken from A. V. Korolev, 2008; details are not shown here). In view of this supersaturation interval and the CCN distributions presented in Figure S1a, it appears that a concentration of activated CCN - and thus N_c - of 100 cm^{-3} is quite realistic for this MARCUS case study.

3. Vertical structure of clouds in the ERA5 reanalysis

Since the previous ERA-Interim reanalysis of the European Center for Medium Range Forecasts (ECMWF), the cloud scheme of the Integrated Forecast Model - which ECMWF reanalyses are based on - has been improved (Forbes & Tompkins, 2011). Specific adaptations have been made for the representation of mixed-phase clouds (Forbes & Ahlgrimm, 2014), particularly regarding the vapor deposition on ice crystals at cloud top. Moreover, the vertical resolution has been substantially increased in ERA5 with respect to ERA-Interim. Despite those improvements, Figure S5a shows that ERA5 in unable to capture thin layers of supercooled liquid droplets at the top of altocumulus during our study case. However, and unlike the ctrl WRF simulation, ERA5 simulates SLW below about 2500 m during the core of the event. However the liquid water path is significantly underestimated compared to radiometer estimations (Figure S5b).

4. Effect of secondary ice production through collisional break-up

Young et al. (2019) underline that the number concentration of ice crystals observed in clouds over the Weddell Sea frequently exceeds the concentration of INPs by several orders of magnitude. Sotiropoulou et al. (2020) show that taking into account the secondary ice production by collisional break-up of iced particles in WRF simulations - a process missing in most atmospheric models - can reconcile modelled ice crystal concentrations with observations. Here we assess to what extent our conclusions regarding the simulation of frontal mixed-phase clouds off the coast of Mawson are changed when accounting for collisional break-up. We performed simulations with the new primary ice nucleation scheme (see section 2.2.1 of the main manuscript) and with the so-called 'FRAG1siz' break-up parameterization (suffix -SIP in simulation names) that yielded a fair agreement between modeled and observed ice concentration over the Weddell sea in Sotiropoulou et al. (2020). This parameterization assumes that ice collisions generate a new fragment if the particle that undergoes fragmentation is larger than 300 μm. Note that secondary ice production through the Hallett-Mossop mechanism is also permitted here. Figure S7a shows that for both vertical grids and as expected, the break-up parameterization significantly increases the number of iced-particles at temperatures higher than -25^{o}C. From this figure one can also gauge how much the new ice nucleation description decreases the number of ice crystals especially at temperatures lower than -20^{o}C.

However, Figure S8 shows that the overall vertical structure of cloud and precipitation above the ship is not dramatically modified when collisional break-up is taken into account (for both vertical grids). When looking more attentively, one can further point out in simulations including break-up:

• a slight increase in precipitation rate (not shown) due to enhanced vapor deposition, aggregation and riming associated with the increase in crystal number (see also panels a and b of Figure S7).

• a decrease in cloud liquid water content, especially during the second part of the event below 3000 m. Inspection of cloud liquid water tendencies shows that such a difference is mostly due to a decrease in droplet activation (less frequent liquid saturation) and to a lesser extent, to an increase in riming.

• a more efficient - and more realistic - low level sublimation after 10 UTC during the last day. This is mostly explained by the overall decrease in hydrometeor size (smaller crystals are more easily sublimed) associated with the increase in number concentration (see panels c and d of Figure S7).

Further observations like measurements of ice crystal concentration would be necessary to assess if the break-up parameterization is truly beneficial to our simulations or not. However, one can already conclude that it does not substantially deteriorate the simulation of thin SLW layers.

References

Bouniol, D., Illingworth, A., & Hogan, R. (2004). Deriving turbulent kinetic energy dissipation rate within clouds using ground based radar. *Proceedings of ERAD*, *281*(285).

Cooper, W. A. (1986). Ice initiation in natural clouds. *Meteor Mon*, *21*, 29–32.

DeMott, P. J., Prenni, A. J., Liu, X., Kreidenweis, S. M., Petters, M. D., Twohy, C. H., ... Rogers, D. (2010). Predicting global atmospheric ice nuclei distributions and their impacts on climate. *Proceedings of the National Academy of Sciences*, *107*(25), 11217–11222.

Doviak, R. J., & Zrnic, D. S. (1993). *Doppler radar and weather observation.* Dover Publications; Second edition.

Forbes, R., & Ahlgrimm, M. (2014). On the representation of high-latitude boundary layer mixed-phase cloud in the ecmwf global model. *Mon Wea Rev*, *142*, 3425–3445.

Forbes, R., & Tompkins, A. (2011). An improved representation of cloud and precipitation. *ECMWF Newsletter*, *129*, 13-18.

Humphries, R. S. (2019). Exhaust identification product for MARCUS project aboard aurora australis 2017/18. *Australian Antarctic Data Centre*, *Ver. 1*. doi: 10.26179/5cf868e1d3414

Kollias, P., Clothiaux, E. E., Ackerman, T. P., Albrecht, B. A., Widener, K. B., Moran, K. P., ... Mace, G. G. (2016). Development and applications of arm millimeter-wavelength cloud radars. *Meteorological Monographs*, *57*, 17.1-17.19. doi: 10.1175/AMSMONOGRAPHS-D-15-0037.1

Korolev, A., McFarquhar, G., Field, P. R., Franklin, C., Lawson, P., Wang, Z., ... Wendisch, M. (2017). Mixed-phase clouds: Progress and challenges. *Meteorological Monographs*, *58*, 5.1-5.50. doi: 10.1175/AMSMONOGRAPHS-D-17-0001.1

Korolev, A. V. (2008). Rates of phase transformations in mixed-phase clouds. *Quarterly Journal of the Royal Meteorological Society*, *134*(632), 595-608. doi: 10.1002/qj.230

Korolev, A. V., & Mazin, I. P. (2003). Supersaturation of water vapor in clouds. *Journal of the Atmospheric Sciences*, *60*(24), 2957-2974. doi: 10.1175/1520-0469(2003)060⟨2957:SOWVIC⟩2.0.CO;2

Lachlan-Cope, T., Listowski, C., & O'Shea, S. (2016). The microphysics of clouds over the antarctic peninsula – part 1: Observations. *Atmospheric Chemistry and Physics*, *16*(24), 15605–15617. Retrieved from `https://www.atmos-chem-phys.net/16/15605/2016/` doi: 10.5194/acp-16-15605-2016

Lothon, M., Lenschow, D., Leon, D., & Vali, G. (2005). Turbulence measurements in marine stratocumulus with airborne doppler radar. *Quarterly Journal of the Royal Meteorological Society: A journal of the atmospheric sciences, applied meteorology and physical oceanography*, *131*(609), 2063–2080.

O'Shea, S. J., Choularton, T. W., Flynn, M., Bower, K. N., Gallagher, M., Crosier, J., ... Lachlan-Cope, T. (2017). In situ measurements of cloud microphysics and aerosol over coastal antarctica during the mac campaign. *Atmospheric Chemistry and Physics*, *17*(21), 13049–13070. doi: 10.5194/acp-17-13049-2017

Roberts, G. C., & Nenes, A. (2005). A continuous-flow streamwise thermal-gradient ccn chamber for atmospheric measurements. *Aerosol Science and Technology*, *39*(3), 206-221. doi: 10.1080/027868290913988

Shupe, M., Brooks, I., & Canut, G. (2012). Evaluation of turbulent dissipation rate retrievals from doppler cloud radar. *Atmospheric Measurement Techniques*, *5*(6), 1375–1385.

Shupe, M. D., Kollias, P., Persson, P. O. G., & McFarquhar, G. M. (2008). Vertical motions in arctic mixed-phase stratiform clouds. *Journal of the Atmospheric Sciences*, *65*(4), 1304–1322.

Sotiropoulou, G., Vignon, E., Young, G., Morrison, H., O'Shea, S. J., Lachlan-Cope, T., ... Nenes, A. (2020). Secondary ice production in antarctic mixed-phase clouds: an underappreciated process in atmospheric models. *Atmos Chem Phys Discuss*, *under review*. doi: 10.5194/acp-2020-328

Young, G., Lachlan-Cope, T., O'Shea, S. J., Dearden, C., Listowski, C., Bower, K. N., ... Gallagher, M. W. (2019). Radiative effects of secondary ice enhancement in coastal antarctic clouds. *Geophysical Research Letters*, *46*(4), 2312-2321. doi: 10.1029/2018GL080551

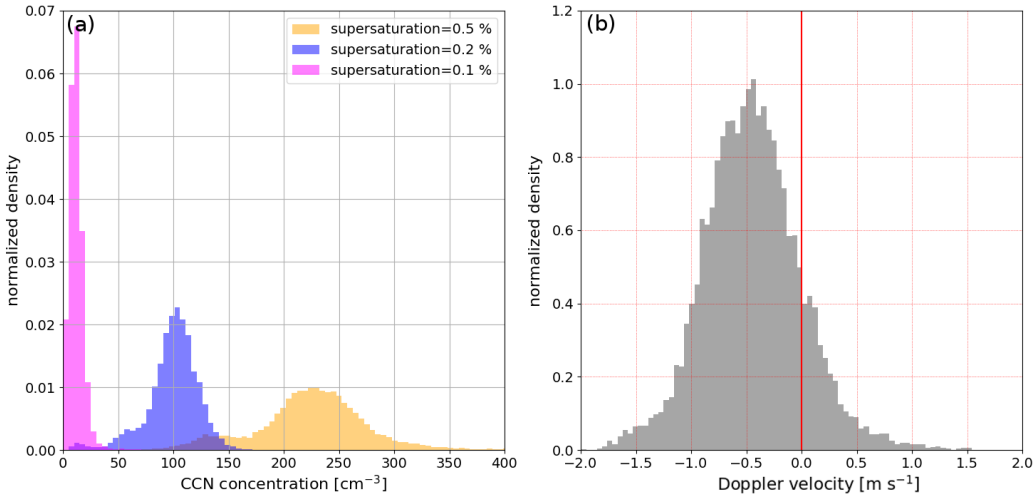

Figure S1. Panel a: CCN concentration distribution at 0.1 % (magenta), 0.2 % (blue) and 0.5 % (orange) supersaturation measured on the Aurora Australis between the 14 and 16 February 2018. Panel b: Distribution of the Doppler velocity measured by MWACR conditioned to regions with presence of SLW identified with the MPL.

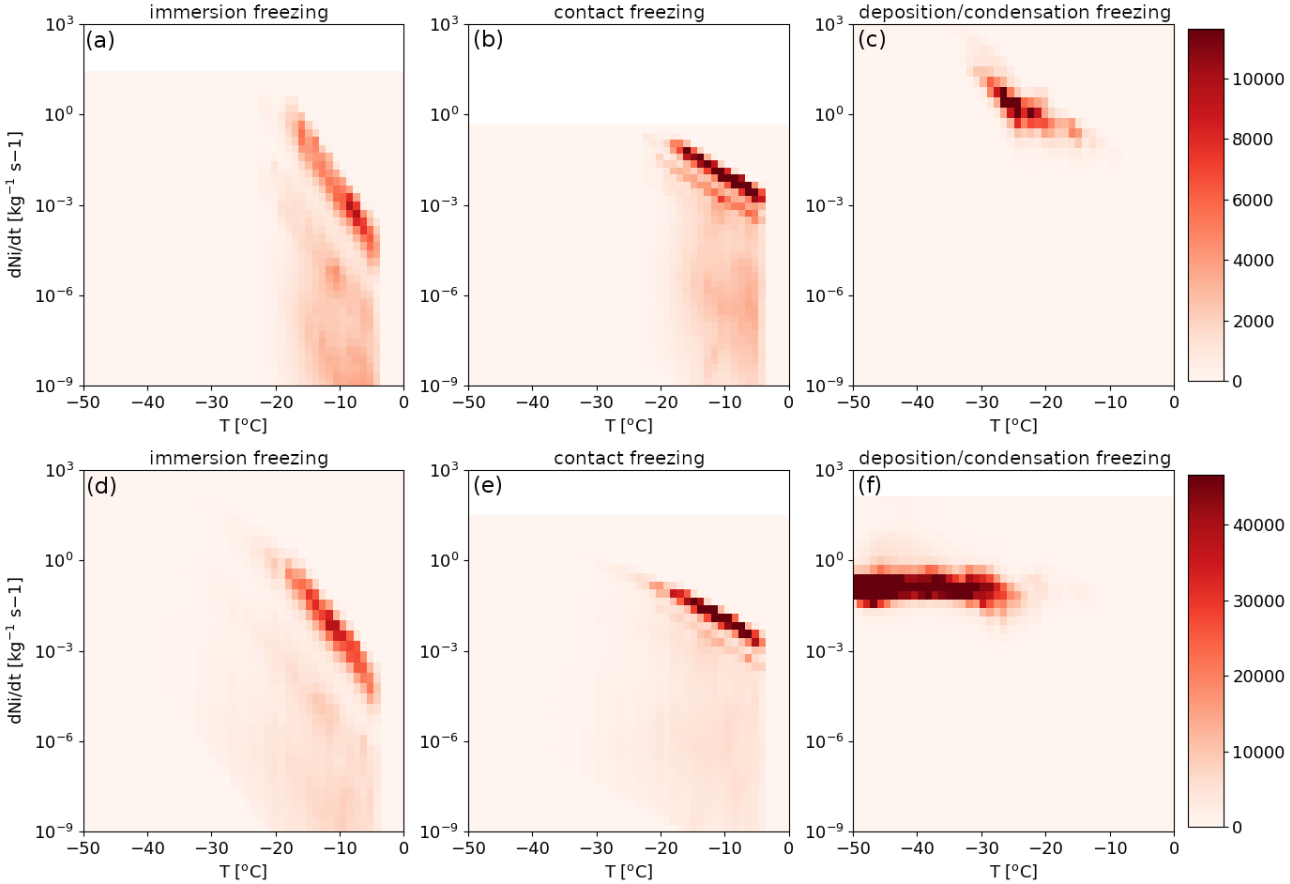

Figure S2. Top row: 2-D histograms of the cloud ice number concentration tendencies associated with each heterogeneous ice nucleation mechanism versus temperature in the ctrl simulation. Bottom row: same as top row but replacing the Cooper (1986)'s INP formulation in the deposition/condensation freezing nucleation parameterization with the formula from DeMott et al. (2010) and assuming an aerosol concentration of 0.1 scm^{-3}.

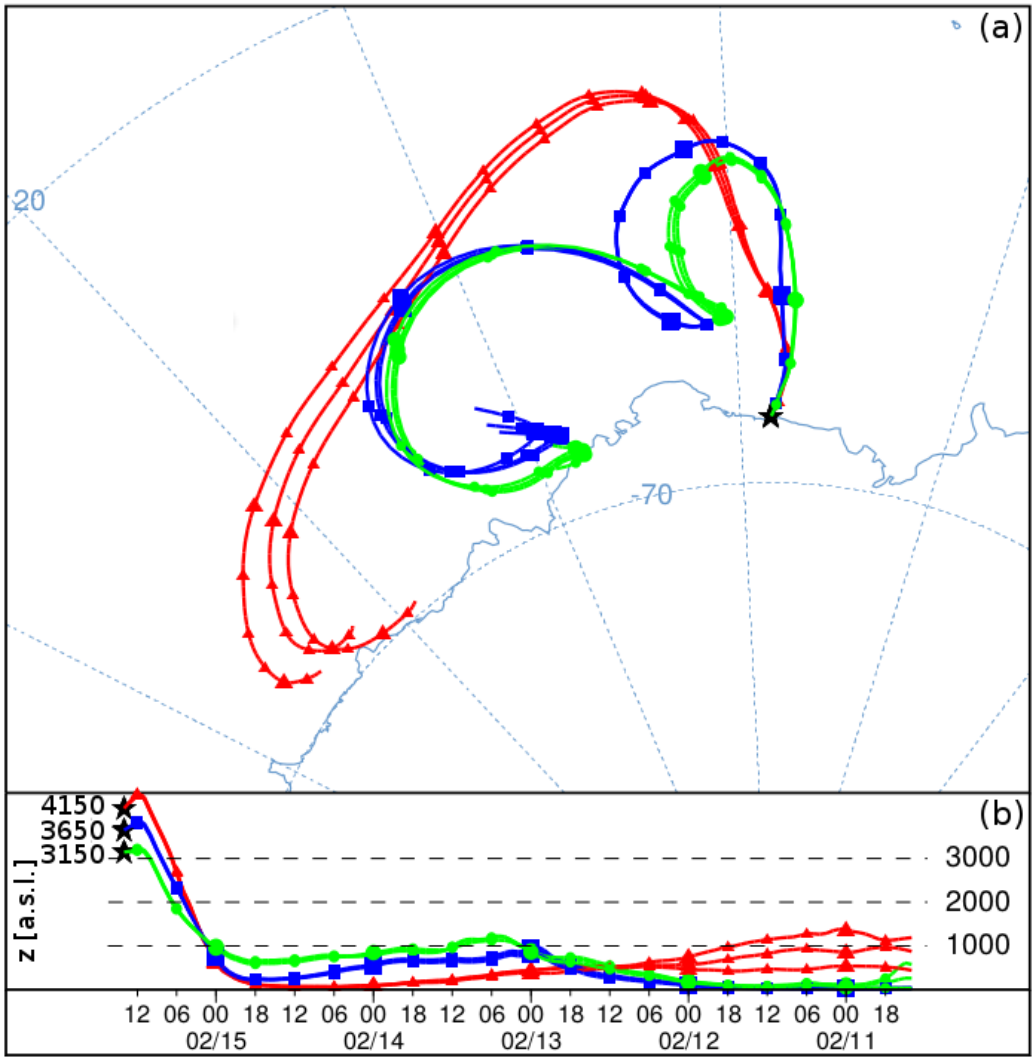

Figure S3. Panel a: Map of 5-day air parcel back-trajectories ending at 1400 UTC, 15 February 2018 (middle of the studied event) at three altitudes (different colors) near cloud-top above Mawson station (black star). The three trajectories of each color correspond to a slight longitude shift of ± 0.5° of longitude around the arrival point. Panel b: temporal evolution of the altitude of air parcels on their way towards Mawson. Back-trajectories were calculated with the HYPLIT modeling system (`https://www.ready.noaa.gov`) using the 0.5° × 0.5° Global Forecast System meteorological data.

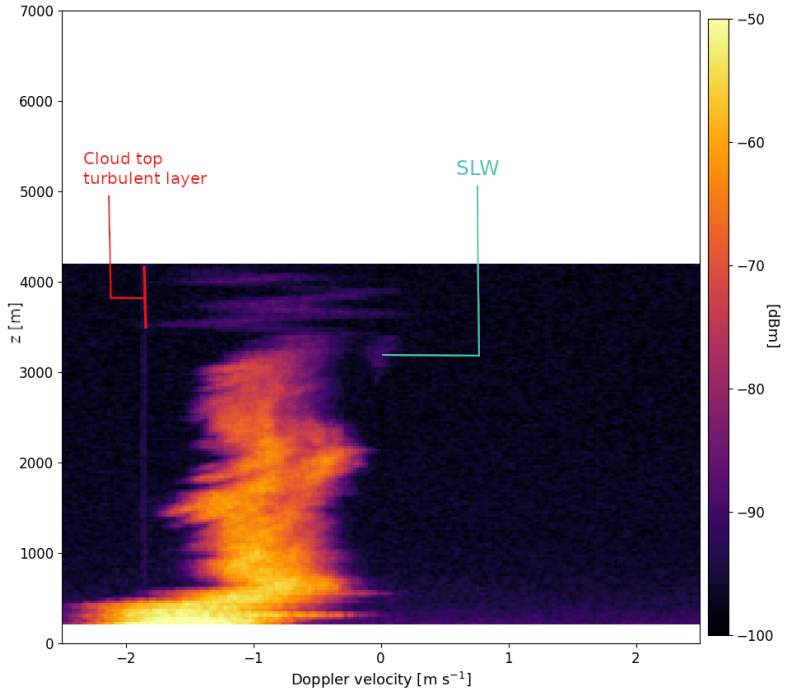

Figure S4. Raw Doppler spectrogram from MWACR measurements at 12:55:31, 15 February 2018. The near-zero Doppler velocity patch at $z \approx 3200$ m indicates the presence of SLW droplets. It is worth mentioning that SLW detection from this spectrogram is not possible in the 3500-4200 m turbulent layer where the Doppler velocity signal is strongly influenced by turbulent eddies.

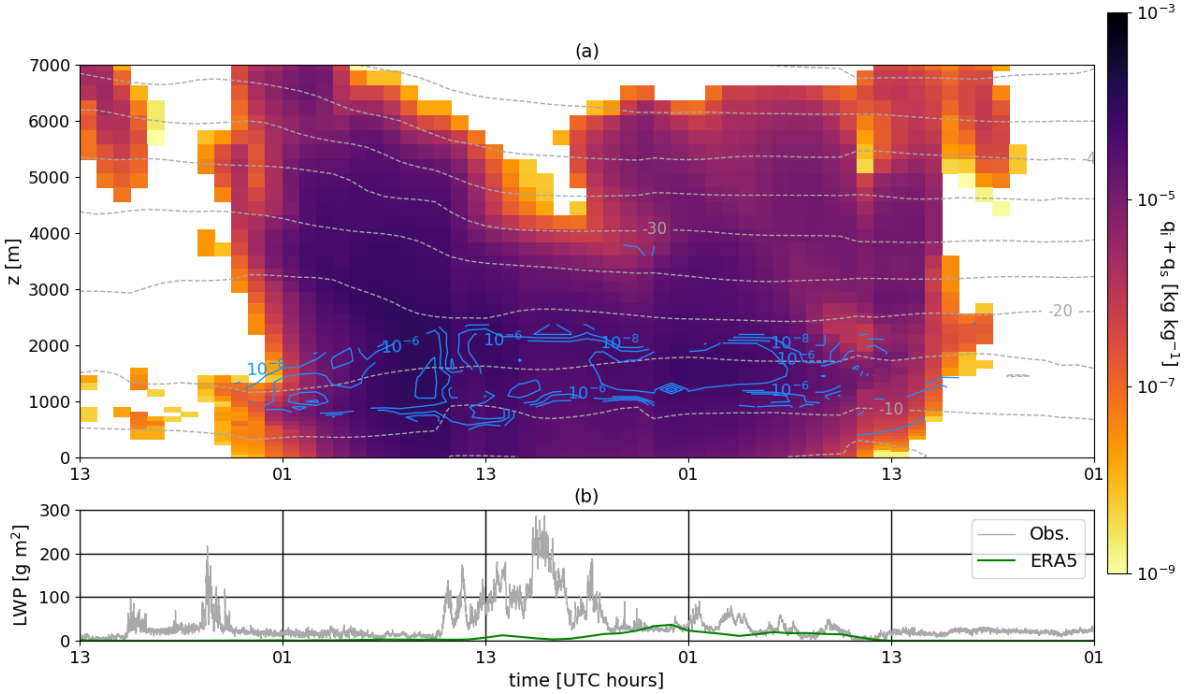

Figure S5. Panel a: Time-height plot of the mass mixing ratio of ice and snow ($q_i + q_s$) above Mawson station and between 14 and 16 February 2018 from the ERA5 reanalysis (shading). Grey (resp. blue) contours show the temperature in °C (resp. the mass mixing ratio of cloud liquid water in kg kg−1). Panel b: LWP time series from radiometer observations (grey line) and from ERA5 (green line).

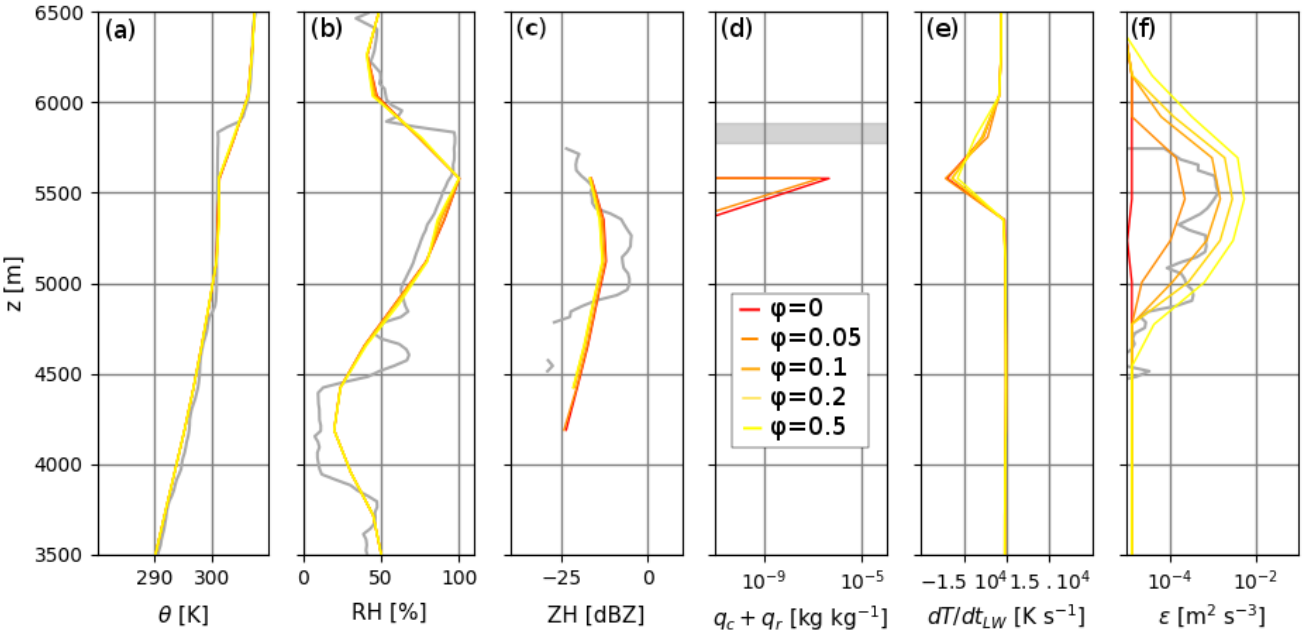

Figure S6. Vertical profiles of the potential temperature (a), relative humidity with respect to liquid (b), W-band radar reflectivity (c), liquid water content (sum of cloud droplets and rain drops, d), longwave radiative heating (e) and rate of turbulent kinetic energy dissipation (f) at 1730 UTC, 14 February 2018. Grey lines refer to observations while red-to-yellow lines refer to WRF simulations with different values of the ϕ coefficient. In panels a and b observational data are from the closest-in-time radiosounding. In panels c and f observations are from MWACR data. In panel d, the grey shading indicates the altitude range where the MPL detects SLW.

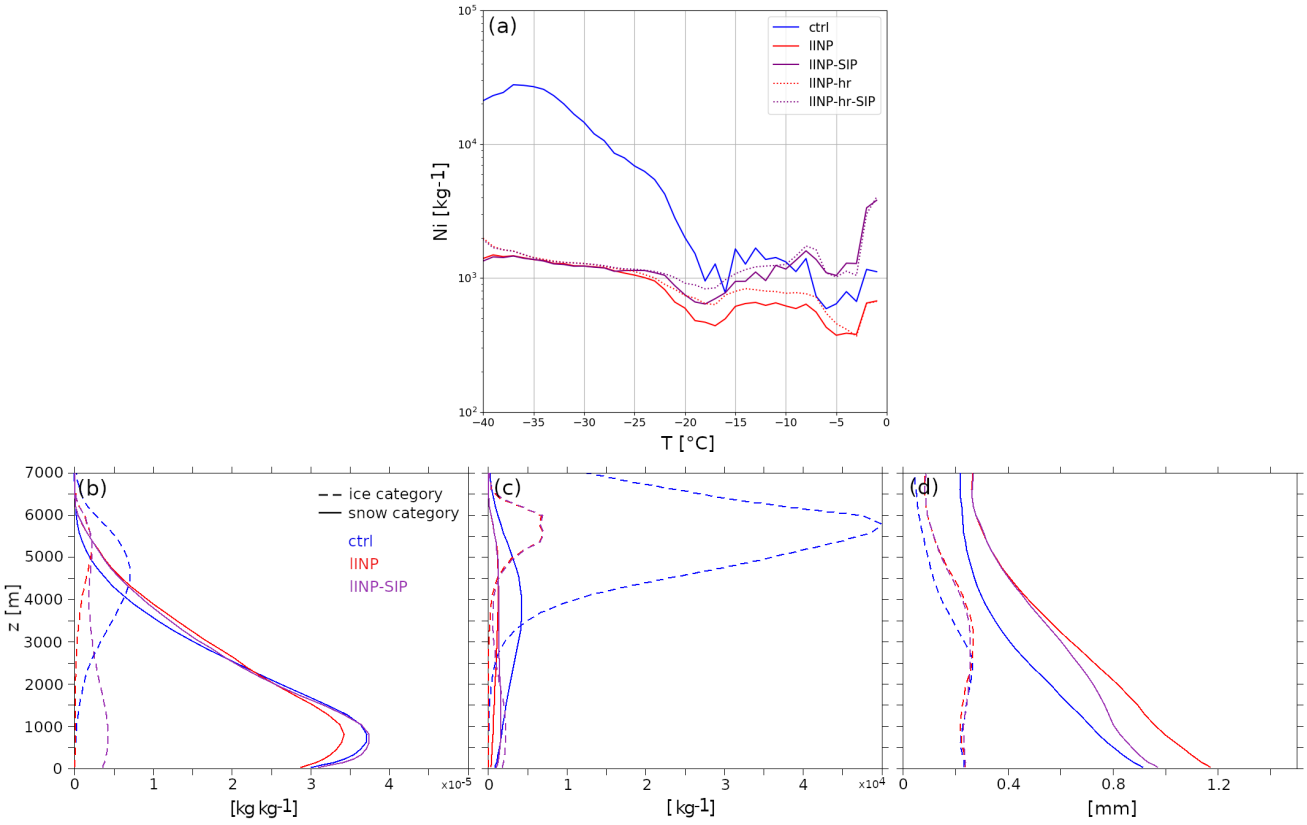

Figure S7. Panel a: Median iced particle number concentrations (cloud ice + snow + graupel) as a function of temperature in 5 different WRF simulations. Data are from all the grid points in the 3-km resolution domain. Panel b-d: Mean vertical profiles of the mass mixing ratio (b), number mixing ratio (c) and mean mass diameter (d) of ice (dashed lines) and snow (solid lines) particles in the ctrl (blue), lINP (red) and lINP-SIP (purple) simulations. The vertical coordinate is the altitude above ground level. Data are averaged over all the model grid points in the 3-km resolution domain and between 12:00, 14 February and 22:00, 16 February. Suffix -SIP in simulation names indicate the use of the break-up parameterization.

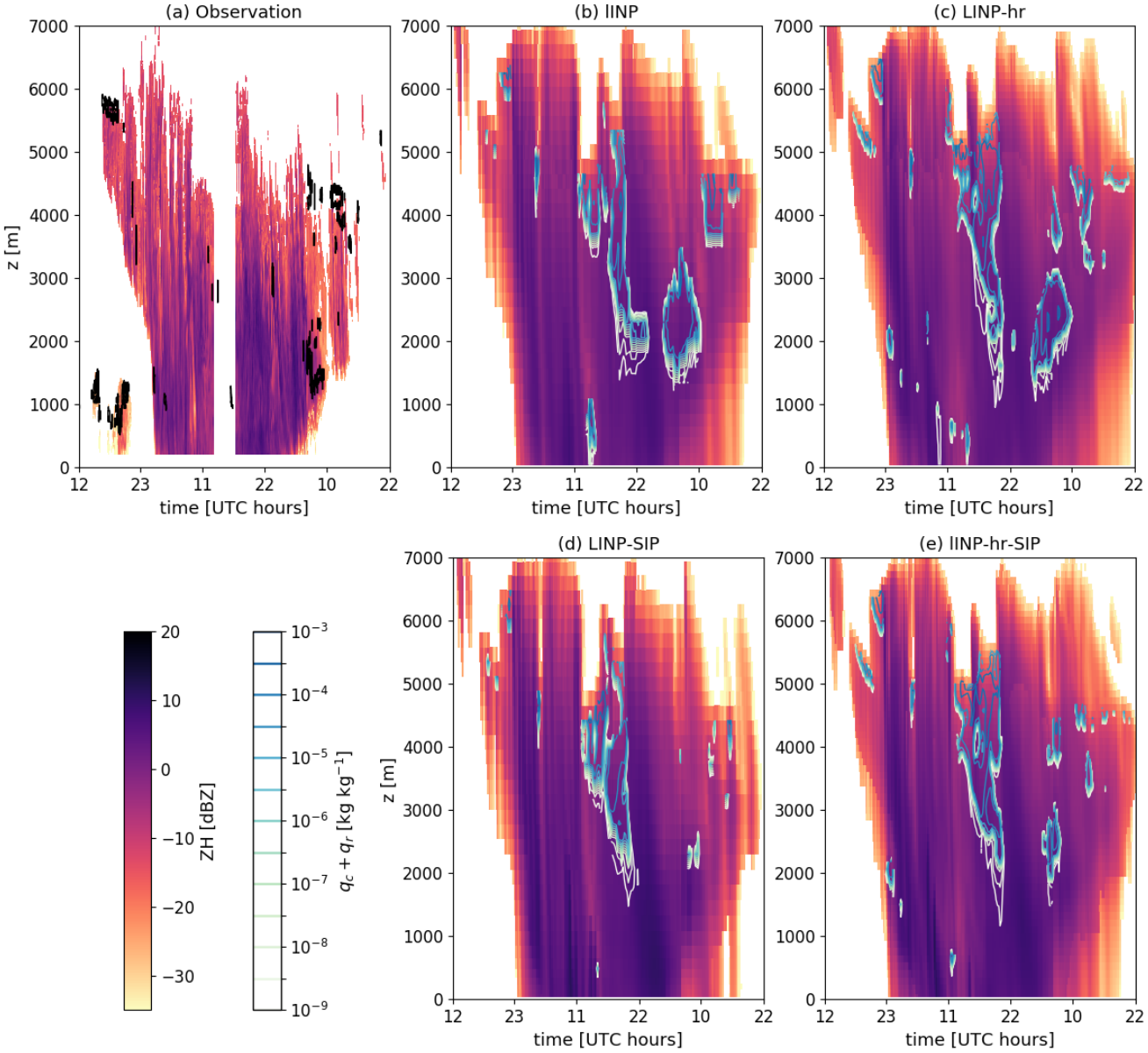

Figure S8. Time-height plot of the W-band reflectivity in MWACR observation (panel a) and as calculated from WRF simulations with the CR-SIM radar simulator (panels b-e). In panel a, black outlines locate regions where the MPL detects SLW. In panels b-e, yellow-to-blue contours show the mass mixing ratio of cloud liquid water (sum of cloud and rain droplets). Suffix -SIP in simulation names indicate the use of the break-up parameterization.